Identification of ferroelectric $HfZrO_2$ from the distinct signature of O 1s spectra in polar and non-polar sublattices

Marius Adrian Husanu, Lucian Dragos Filip, Cristina Florentina Chirila, and Dana Georgeta Popescu*
National Institute of Materials Physics, Atomistilor 405A, 077125 Magurele, Romania

(Received 25 June 2025; accepted 29 January 2026; published 2 March 2026)

$HfZrO_2$(HZO) is a promising ferroelectric material compatible with CMOS technology, retaining functionality at nanometer-scale thicknesses. Its ferroelectricity arises from metastable polar phases—orthorhombic ($Pca2_1$) and rhombohedral ($R3m$)–coexisting with the thermodynamically stable, non-polar monoclinic phase ($P2_1/c$). Accurate quantification of these coexisting phases is essential for optimizing device performance. Here, we use first-principles calculations to estimate core-level shifts in the O 1s X-ray photoelectron spectroscopy (XPS) peak, revealing a distinct, up to 0.84 eV higher binding energy component for oxygen atoms in the polar sublattice compared to those in non-polar environments. These shifts incorporate both initial and final state effects in photoemission. Experimental validation through X-ray diffraction (XRD) and XPS on HZO films with varying phase composition confirms our predictions. Our findings provide a clear, spectroscopically accessible fingerprint to distinguish polar and non-polar phases in HZO via O 1s XPS analysis, offering a practical tool for phase quantification and enabling targeted integration of ferroelectricity in advanced nanoelectronic devices.

DOI: 10.1103/h2lj-slbg

I. INTRODUCTION

$HfZrO_2$(HZO) is a versatile and promising ferroelectric (FE) material, with the ferroelectricity subsisting down to unit cell thickness [1–3]. This makes HZO attractive for scaling down devices and, coupled with the requirement of energy saving in modern electronics, promotes it as a material for next-generation devices.

HZO as well as the parent compound HfO_2 experience phase transition from the stable, monoclinic one [4] (m, $P2_1/c$) at room temperature, going through the tetragonal (t, $P4_2/nmc$) toward the cubic phase (c, Fm-3m) at high temperatures.

There also exist several polar phases of hafnia and HZO, such as the orthorhombic (o, $Pca2_1$, and $Pmn2_1$) and rhombohedral ($R3m$) [5]. The emergence of both polar and antipolar distortions [6,7] separated by only small energy barriers [8,9] defines rich possibilities to design functionality [10] based on the overlap in the phase space of Hf-based polymorphs as a function of strain [11–13] and doping [14–17].

Ferroelectricity in HZO is identified in its polar phases, common to HfO_2 as well, where Hf as a 5d element defines Hf–O ionic bonds and impose the large band gap of HfO_2. Among all FE phases, the most plausible from an energetic perspective is that belonging to $Pca2_1$ [7]. It consists of alternating fourfold-coordinated (4F) and threefold-coordinated (3F) oxygen atoms, where the asymmetric displacements of the 3F oxygen atoms break the inversion symmetry, generating the macroscopic spontaneous polarization [18,19].

Importantly, the inversion symmetry breaking in HZO polar phases is mainly due to local displacements of oxygen anions. This illustrates how hafnia-based ferroelectrics are more susceptible to oxygen vacancies [20,21] compared to their perovskite counterparts. It has been suggested that this feature may open the possibility of bypassing the well-known empty-shell requirement [22] of ferroelectric perovskites, potentially leading to the design of new materials with coexisting ferroic phases [7].

The $Pca2_1$ phase consists of two sublattices: a symmetric one and a polar one [19]. This peculiarity of the unit cell is an important ingredient that allows ferroelectricity to survive down to monolayer thicknesses.

However, the polar phases of HZO do not represent minima in the phase diagram; hence, in bulk they are not energetically favorable. Strategies to induce ferroelectricity include defect and vacancy formation [17] or doping, for example, with Si [23,24], Al [25], Y [26], or alloying [27]. The assistance of the epitaxial strain induced by the substrate [5,28,29] accompanied by non-equilibrium thermal treatment—rapid thermal annealing (RTA) [30] and/or sudden cooling [14] that quenches the FE phase—are other strategies, which so far have been successfully employed.

Often, HZO results in varying amounts of coexistence between the polar and non-polar phases. The coexisting m and o phases raises, for example, the question of how to quantitatively establish the amount of each phase. Among the techniques previously employed, transmission electron microscopy (TEM) is only local, while X-ray diffraction (XRD), by collecting the signal from a large volume, including one or several interfaces often complicates the accurate separation and quantitative determination of each crystalline phase when their peaks overlap.

X-ray photoelectron spectroscopy (XPS) measures the kinetic energy of a photoelectron excited with X-rays or UV light. The outgoing electron from one of the occupied

*Contacy author: dana.popescu@infim.ro

energy levels of the atom is a fingerprint of the chemical state, bonding nature, or environment. Moreover, XPS is a surface sensitive technique, which probes a thickness of 2–5 nm; hence, it is highly relevant for such thin films as HZO. Although routinely used in the characterization of bulk and thin film materials, presently there is no experimental prescription, which allows identifying the different crystalline phases of HZO in the XPS data.

Here, by addressing the distinct signature of O 1s core levels shift in the FE and non-FE state, we formulate a general recipe to quantitatively assess the amount of each phase in HZO.

By using DFT calculations, we will estimate the relative core-level shifts (CLS) of the O atoms lying in the polar sublattice of FE *o*-HZO, compared to oxygens lying in the symmetric one, thus establishing whether X-ray photoemission can be used as a probe for establishing the amount of *o* and *m* phases in HZO.

II. COMPUTATIONAL AND EXPERIMENTAL METHODS

A. Pulsed laser deposition

All samples were fabricated using the pulsed laser deposition (PLD) technique in a high-vacuum chamber equipped with a KrF excimer laser ($\lambda = 248$ nm). Commercial ceramic targets were used for both layers: the LSMO ($La_{0.70}Sr_{0.30}MnO_3$ and $La_{0.67}Sr_{0.33}MnO_3$) targets were supplied by Praxair, while the HZO ($Hf_{0.5}Zr_{0.5}O_2$) target was provided by Mateck. The laser fluence, repetition rate, substrate temperature, and ambient pressure were carefully controlled to ensure reproducibility and high-quality thin film growth. The target-to-substrate distance was fixed at 5 cm for all depositions. The films were grown on single-crystal (001)-oriented $SrTiO_3$ (STO) substrates with a TiO_2-terminated surface, prepared to ensure atomically flat morphology and promote epitaxial growth of the LSMO bottom electrode.

For the LSMO layer, deposition was carried out at a substrate temperature of 775 °C, with a laser fluence of 1 J/cm^2 and a repetition rate of 5 Hz. The deposition was carried out in an oxygen atmosphere, with the partial pressure set at 0.15 mbar. The HZO films were deposited at a substrate temperature of 800 °C using a laser fluence of 1.1 J/cm^2 and a repetition rate of 2 Hz. The oxygen partial pressure during deposition was kept constant at 0.1 mbar for all samples. The number of laser pulses applied for the HZO layers was 233 for HZO1, 333 for HZO2, and 500 for HZO3. The estimated thickness from the number of pulses, based on prior calibrations, is ∼2 nm for HZO1, ∼3 nm for HZO2, and ∼5 nm for HZO3.

Sr doping for the LSMO buffer of HZO1 sample was $x = 0.30$, while the LSMO used as buffer from HZO2 and HZO3 sample was from a different target with Sr content $x = 0.33$.

Immediately after the HZO deposition, the substrate temperature was kept at 800 °C while oxygen was introduced at maximum flow rate into the chamber until a pressure of 0.3 mbar was reached. The samples were then cooled down to room temperature at a controlled rate of 5 °C/min.

HZO1-Ox sample was obtained from half of the HZO1 sample by post-deposition annealing treatment in oxygen at a temperature of 800 °C and pressure of 1 bar in order to evaluate the effect of post-growth oxidation on phase composition and electrical performance.

B. First-principles calculations

DFT calculations were performed using the QUANTUM ESPRESSO (QE) plane wave package [31,32] and local density approximation (LDA) for the exchange and correlation functional in the PZ parametrization [33]. We used norm-conserving pseudopotentials generated with the scalar-relativistic version of the ONCVPSP [34] software. The following electron configurations were used: Hf: $4f^{14}5p^65d^26s^2$, Zr: $4p^64d^25s^2$, O $2s^22p^4$. We employ the atomic coordinates of HfO_2 in the $Pca2_1$ orthorhombic space group from the Materials Project [35] and constructed $2 \times 2 \times 2$ supercells with 96 atoms. The total energy and force per atom were converged to less than 10^{-3} eV/atom. Zr atoms were stoichiometrically inserted to account for the experimental value Hf:Zr = 0.5:0.5. Relaxation of the unit cell and of the internal coordinates were performed on an automatically generated, uniform $4 \times 4 \times 4$ Monkhorst–Pack k-mesh [36]. Further self-consistent followed by non-self-consistent calculations were performed with $8 \times 8 \times 8$ k-meshes. Relaxations were performed by using 100 Ry kinetic-energy cutoff, while self-consistent calculations were performed with 80 Ry kinetic-energy cutoff for the plane waves.

The chemical shifts of O 1*s* core level were calculated by using an O pseudopotential generated with a core hole on the 1*s* level by using the same software.

The final state effects were estimated from the total energy difference between self-consistent calculations when the core-hole O atom is placed in the polarsymmetric sublattice of HZO.

The initial state effect contributions at CLS are estimated through computing the $\langle\psi^*|V-V_h|\psi\rangle$ value in the Kohn-Sham basis.

Drawing of the HZO supercell was done by using the VESTA software [37].

C. X-ray photoelectron spectroscopy (XPS)

XPS measurements were performed on a Kratos AXIS Ultra DLD, employing a semispherical analyzer with a 0.6 eV spectral resolution, for XPS investigations. The monochromatized source of the Al Kα1 (1486.74 eV) radiation had a spot size of 0.7 mm. Using a hybrid mode for the lens and a slot aperture, the survey was measured with a pass energy of 160 eV, the high resolution one with 40 eV, and the source power of 144 W (12 kV × 12 mA). A flood gun neutralizer (filament current 1.8 A, charge balance 2.7 V, filament bias 1.0 V) was used to partially compensate for the charging of the samples. During the measurements, the analysis chamber's pressure was better than 10^{-9} mbar. The spectra were fitted in the IGOR Pro 9.05 software.

D. X-ray diffraction (XRD)

A 40 kV × 40 mA Cu X-ray tube was used in a Rigaku-SmartLab diffractometer to perform X-ray diffraction measurements. The patterns were obtained using a 2-bounce

Ge(400) monochromator. We took into account the sample's cutoff and aligned it following the substrate's STO 002. In the 2Theta = 18−37° region, 2 Theta-Omega patterns were measured at a speed of 1 gpm with a step size of 0.02.

E. Electrical measurements

All capacitance measurements were conducted at room temperature and 100 kHz frequency, using a HIOKI 3235 LCR meter and a Keithley 5234 electrometer. The capacitance values used to calculate the dielectric constants were taken at zero bias voltage to capture the intrinsic dielectric response of the films without field-induced contributions.

III. RESULTS AND DISCUSSION

The XPS process consists of ionizing a core-level electron by excitation with UV or X-ray radiation and measuring its kinetic energy. The energy of the outgoing electron serves as a fingerprint of the chemical environment it originates from, allowing XPS to establish surface stoichiometries and chemical state of the atoms in the material.

Conceptually, we may decouple the photoemission process in two stages:

(i) the *initial state*, which represents the unperturbed system, before the excitation of the core-hole electron from the core-level *n*.

(ii) the *final state,* which contains the system in the excited state, with a core-hole on the level *n* where the electron is extracted from.

The system excited in the final state, with a core-hole on the level *n*, may further experience many-body effects due to the interaction of the core-hole with the rest of the electrons and inner relaxation effects. Experimentally, both initial and final state effects are relevant to the total CLS.

Estimating the contribution of the final state effects at the O 1*s* core level shifts involves self-consistent calculations in the HZO supercells where the core-hole atom is placed in the two different environments. The relative shift of the O 1*s* core level in the symmetric, non-polar sublattice with respect to the polar sublattice is given by the difference between the total energies of the two configurations.

The initial state contribution at CLS is given in the frozen approximation picture by Koopman theorem [38] and results from calculating the expectation value of the reference and excited pseudopotentials in the Kohn-Sham basis.

Instead of computing absolute binding energies, an approach that is susceptible to large deviations from the experimental values [39], we limit to computing the binding energy difference between the oxygen atoms lying in the symmetric and polar sublattice of HZO. Moreover, unlike other approaches that involve calculations in the so-called "(Z+1)" methodology [40,41] with core-hole pseudopotential generated from atoms with Z+1 nuclear charge, accompanied by the removal of an electron from the core level in order to reproduce the XPS effect, our approach relies on the same atomic species (with and without core-holes), thus minimizing any possible artifacts derived from modifying the nuclear potential.

Our theoretical value, containing the combined initial and final state effect, for the O 1s CLS of the core-hole oxygen in the two sublattices of HZO is ∼0.84 eV, with the component in the polar sublattice at higher binding energies with respect to the O 1s in the symmetric sublattice.

The relative shift contains both the contributions of final state effects (0.44 eV) and initial state effects (0.40 eV). We also performed computations considering the complete screening of the core-hole on the O 1s level by embedding the supercell in a uniformly charged environment, which compensates the resulting charging in the oxygen deficient environment. The correction to the final state effects contribution of CLS is negligible, of 0.04 eV only.

In Fig. 1(a), the HZO supercell is given, indicating the two configurations considered in the calculations of the CLS. Figure 1(b) presents the XPS picture expected from our DFT calculations, with the fine structure of the O 1s peak featuring two components: one at lower binding energies (LBE) summing up the contribution of oxygens from the symmetric sublattice of *o*-HZO and (eventually) that of the oxygen atoms from non-polar phases.

Since the monoclinic phase is non-polar, it is reasonable to assume that its CLS contribution overlaps the signature of O 1s from the symmetric sublattice of the *o* phase. The other component, shifted by 0.84 eV toward higher binding energies (HBE), corresponds to the O in the FE state of *o*-HZO.

We verify this assumption by presenting in addition to the orthorhombic phase, the calculated CLS for the most common, non-polar states of HZO. The cubic, tetragonal, and monoclinic phases [Fig. 2(a)] were considered since they are all connected during the transition from the high temperature, cubic phase, to the tetragonal state, and the stable, non-polar *m*-HZO phase through the orthorhombic, *o*-HZO metastable state.

In Fig. 2, the unit cells of the corresponding structures taken from the Materials Project database [35,42,43] are presented. Their free energy landscape [Fig. 2(b)] is presented in the increasing order of their stability: cubic, tetragonal, orthorhombic, and monoclinic. The tetragonal phase features an incipient ferroelectric character due to the antidistortive instability resulting from the rotation of the oxygen cage [44].

While *o*-HZO has two distinct oxygen sublattices in the form of inequivalent O sites defined by symmetry of the polar displacement, T and m phases distribute their O atoms differently. In the tetragonal phase the fourfold coordination of the O atoms define either apical or equatorial position with respect to Hf, Zr while in the monoclinic phase, the coordination of O atoms is in the form of alternating 3-fold and 4-fold coordination. None of the two phases can be exactly mapped onto the o-HZO phase. Because of this mismatch, initial-state electrostatics and final-state screening pathways of each O site in the *m*/*T* phase cannot be directly associated with the FE or symmetric sublattices of the orthorhombic lattice. This is the reason for the observed dispersion of CLS either toward lower or higher binding energies: ±0.19 eV and ±0.095 eV for respectively the initial and final state effects in *T*-HZO and ±0.39 eV for the contribution of the initial state in *m*-HZO. Even though the site-by-site correspondence fails, the phase averaged chemical environment is still systematically weaker in *c*/*T*/*m* phases compared to *o*-HZO. Consequently,

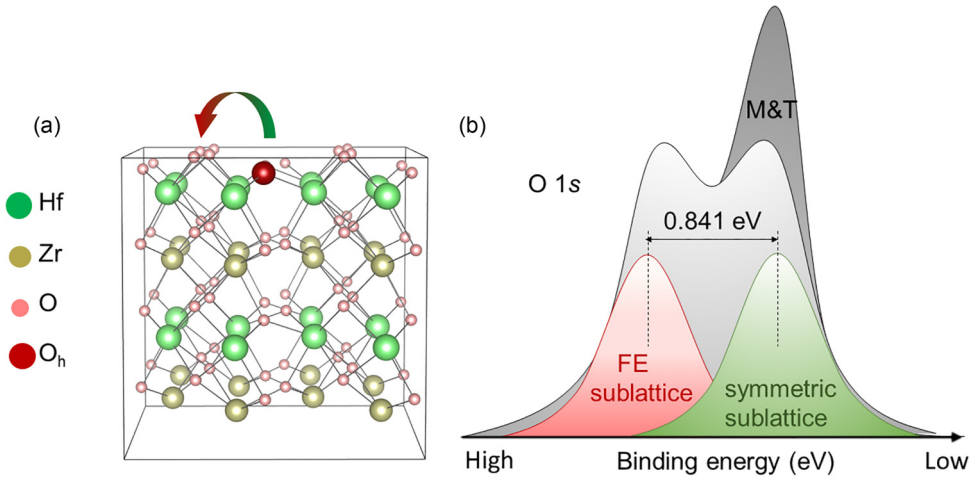

FIG. 1. $Hf_{0.5}Zr_{0.5}O_2$ supercell, with the core-hole oxygen placed in the polar and centro-symmetric supercell (a). The picture is derived from DFT calculations with the O 1s XPS spectrum featuring two components: one derived from O atoms in the FE sublattice at higher binding energies and the other derived from O in the centro-symmetric sublattice at lower binding energies (b).

the CLS of *c*/*T*/*m* phases lie all toward lower binding energies compared to the *o*, FE state.

In order to experimentally assess our predictions, we prepared HZO samples grown in conditions, which favor the stabilization of the FE state and HZO where the *m* phase, non-FE state is predominant. Table I systematically collects the relevant parameters used to tune the crystalline phase of our HZO films.

Figure 3(a) indicates the XRD pattern obtained on HZO grown on $La_{1-x}Sr_xMnO_3$ (LSMO, $x = 0.3$) using $SrTiO_3$ as a substrate (HZO1, blue line) and of the same sample after oxygen annealing (HZO1 - Ox, red line). The XRD data of as-prepared HZO1 indicates that the orthorhombic phase is dominant, while upon oxygen annealing, the sample transitions toward the thermodynamically stable, monoclinic phase.

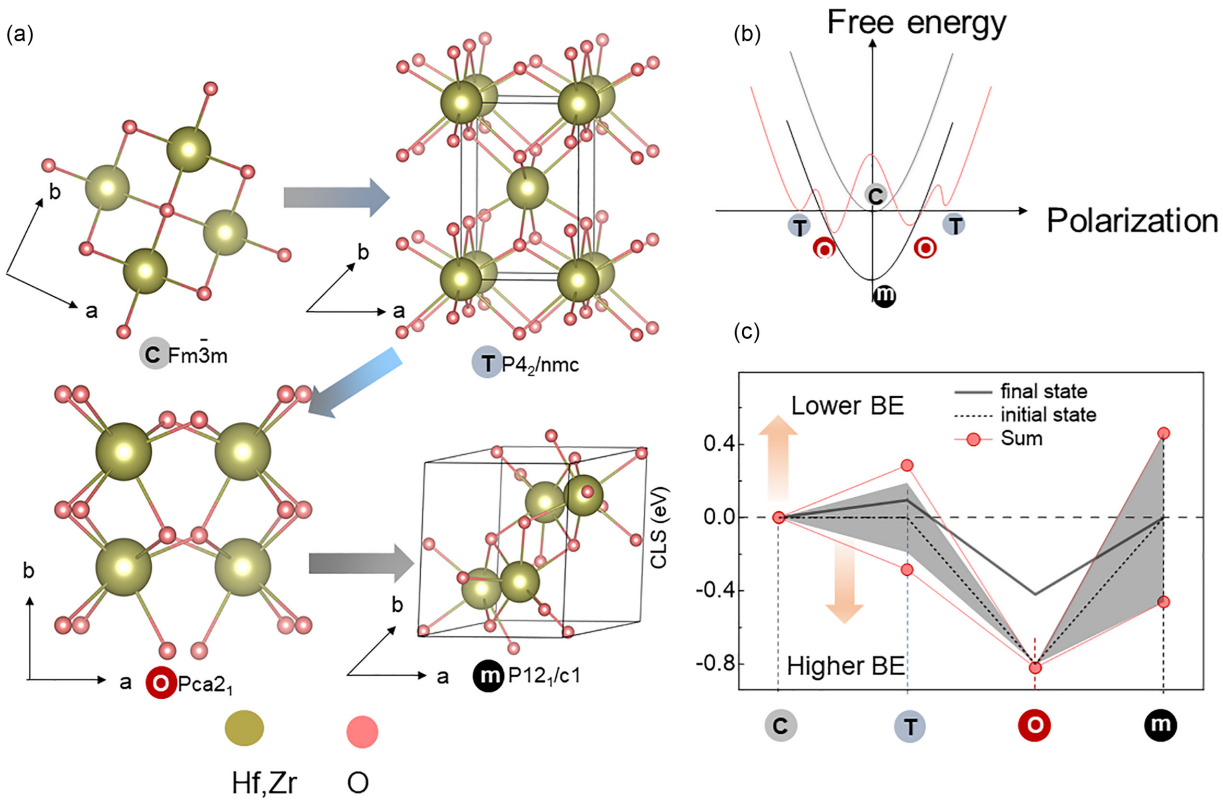

FIG. 2. DFT-calculated core level shifts (CLS) for different crystalline phases of $Hf_{0.5}Zr_{0.5}O_2$(HZO). The cubic (*c*), tetragonal (*T*), orthorhombic (*o*), and monoclinic (*m*) phases of HZO displayed in (a) define the characteristic free energy signature sketched in (b). The calculated CLS for each phase is presented in (c).

TABLE I. Tuning parameters in HZO film preparation.

	HZO1	HZO1 - Ox	HZO2	HZO3
Thickness	2.45 nm	2.45 nm	3 nm	5 nm
Substrate	LSMO, $x = 0.3$	LSMO, $x = 0.3$	LSMO = 0.33	LSMO = 0.33
Treatment	–	O_2 Post-anneal	–	–

The transition between the *o* and *m* phases identified in XRD corresponds to distinct signatures in the XPS spectra. They are presented in Fig 3(b) where the O 1s XPS spectra recorded on the same samples indicate, in addition to the contamination component at 531.5 eV, a clear asymmetry of the main peak at ∼529 eV, further developing toward LBE in *m*-HZO sample. This well correlates with the image established in our DFT calculations where the distinct contribution of oxygen atoms in the polar and symmetric sublattices are separated by ∼0.8 eV [Fig. 1(b)].

The coexistence of *o* and *m* HZO is in our case expected since the HZO preparation involves a protocol where *o*-HZO, normally unstable, is quenched by a combination of growth in oxygen deficient conditions and rapid cooling (see Sec. II). Allowing the recovery of the ideal stoichiometry by oxygen annealing also results in its shift across the phase diagram [4,10] toward the thermodynamically stable phase (i.e., *m*, $P2_1/c$) identified in our XRD measurements through its (002) peak at 34.2°. Its development in the O-annealed HZO1 at the expense of the almost disappearing (111) peak of *o*-HZO at 29.9° indicates the transformation of the *o* phase into the *m* one. In addition, the monoclinic reflections observed after oxygen annealing (m(–111) and m(002)) are consistent with non-epitaxial grains with multiple out-of-plane orientations, fully consistent with the o → m transition [45].

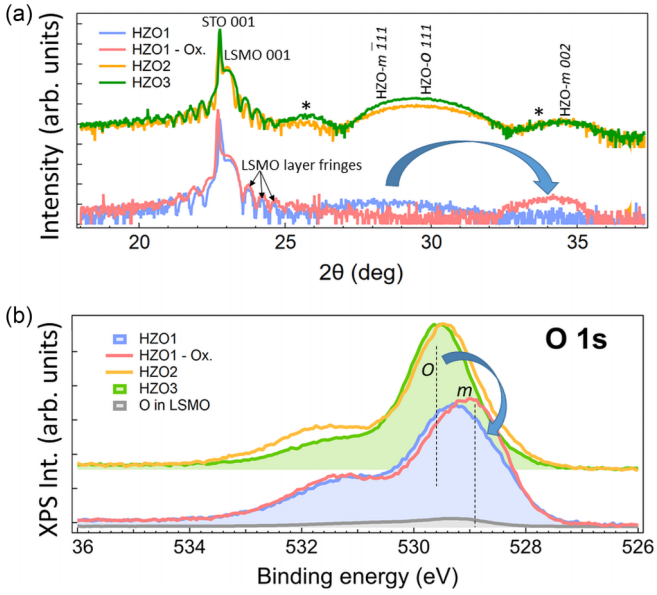

FIG. 3. Experimental $Hf_{0.5}Zr_{0.5}O_2$ XRD (a) and X-ray photoemission (b) on HZO thin films. The gray line in (b) is the O 1s spectrum of LSMO considering the attenuation effects of the top HZO layer. Black stars in (a) represent the HZO fringes.

The simulation of the XPS experimental spectrum with three Voigt lines in Figs. 4(a) and 4(b) for the corresponding samples presented in Fig. 3, HZO1 and HZO1 - Ox, allows for a quantitative assessment of the two coexisting (*o* and *m*) phases in each of the samples. The fit of the XPS data has been performed by constraining two components with the same width into the main peak, separated by at least 0.4 eV, and allowing their amplitude to vary.

For all the samples, the energy separation between the monoclinic component and the contamination component remained the same ∼2.3 eV.

The integrated peak amplitudes corrected by the atomic sensitivity factors are used to establish the amount of *o*-HZO and *m*-HZO as follows:

$$\%o = A_1/[A_1 + (A_2 - A_1)], \quad (1)$$

$$\%m = (A_2 - A_1)/[A_1 + (A_2 - A_1)], \quad (2)$$

where $A_1 = A_{\mathrm{FE}(o)}$ is the area of the O 1s component at high binding energies corresponding to oxygen atoms in the polar sublattice, and $A_2 = A_{\mathrm{sym\,(o)+m}}$ is the area of the O 1s component at LBE corresponding to oxygens in the symmetric sublattice and in the monoclinic phase.

The obtained values are given in Table II.

The analysis of the XPS data reveals that the as-prepared HZO1 sample contains a majority (66.75%) *o,* FE phase—a fact which is supported by our electrical measurements, coexisting with 33.25% *m*-HZO. Notably, for the O_2-annealed HZO, the butterfly-shaped C-V characteristic is absent, in accordance with the drop of the *o* phase to ∼35% compared to the non-polar *m* phase (65%) established in our analysis of the XPS data. The electrical measurements are presented in Fig. S3 from Supplemental Material [46], which includes Refs. [47–49].

The result suggests that the remaining ferroelectric phase is insufficient to sustain polarization switching, and that the film behaves predominantly as a linear dielectric, dominated by the non-polar monoclinic phase.

We also briefly discuss the transferability of our recipe for determining the amount of polar and non polar phase from the XPS spectra (in our case of coexisting *o*-HZO and *m*-HZO) by extending it to other HZO films prepared on electrodes with different hole doping.

TABLE II. Amount of o-HZO and m-HZO from the XPS data.

	HZO1	HZO1-Ox.	HZO2	HZO3
%*o*	66.75	34.12	76.34	93.08
%*m*	33.25	65.88	23.65	6.91

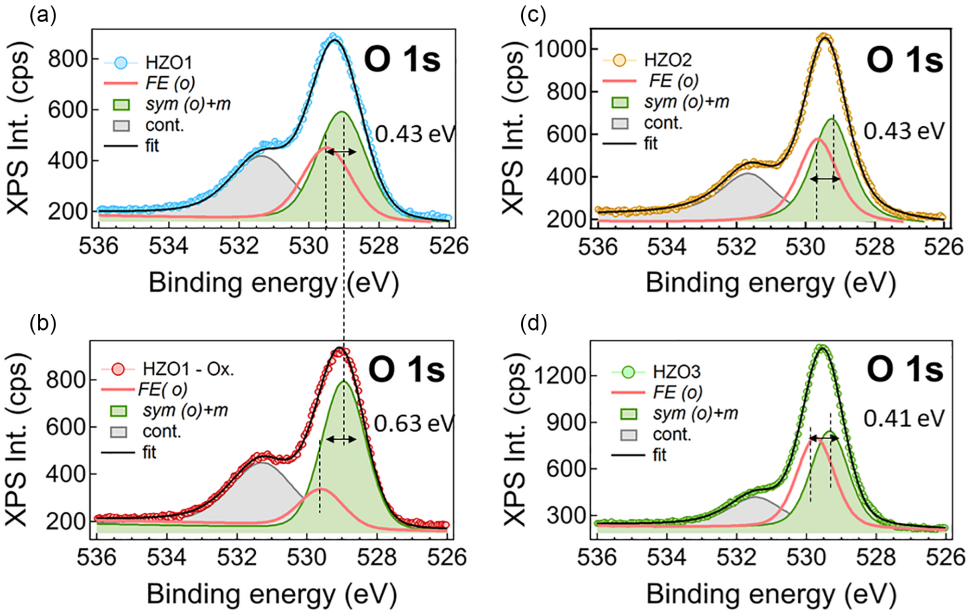

FIG. 4. Simulation of the experimental XPS data with Voigt lines. O 1s spectrum of as-prepared HZO1 (a) and O-annealed HZO1 (b) grown with $La_{1-x}Sr_xMnO_3$ - LSMO ($x = 0.3$) bottom electrode.

It is well established that interface formation between top or bottom electrodes and FE materials occurs with mutual impact on their electronic structure [50–53]. The mechanisms derive from particular band alignment when joining materials with different work functions [54,55], accompanied by charge depletion or accumulation close to the contact region in order to compensate for the depolarizing fields in the FE [56]. In this sense, there is a direct correlation between higher bottom doping of electrodes and the robust ferroelectricity of the adjacent layers [13,48]. Our LSMO buffer layers used as electrodes, as hole-doped materials, feature the largest conductivity for the optimal doping in the half-metallic state around $x = 0.4$ while for smaller Sr content it gradually transitions toward an insulating state close to $x \sim 0.125$ [57].

On the other hand, stabilizing the FE involves a synergy between strain and engineered off-stoichiometry already in the initial growth stage in order to compensate for the particularly strong depolarizing fields of thin films [58–62]. In particular, strategies to enforce the FE state of HZO in the *o*-FE phase involve the combined contribution of strain [11–13], non-equilibrium thermal treatment [30], and/or dopants in the form of impurities [14]. For HZO, *p*-type dopants (within the FE or at their interfaces) seem to ideally enforce the FE state [10]. In this logic, the higher hole-doping of the substrate should better enforce the stabilization of the *o* phase of HZO [12]. Conversely, we hypothesize that the metallic electrode in contact with HZO in FE state should be more hole-depleted compared to the same interface where HZO is in non-polar and non-FE state.

Hence, in order to validate our *o*/*m* estimation protocol derived from the analysis of O 1s XPS spectra, we prepared two additional samples using as a conductive buffer LSMO with higher hole doping, $x = 0.33$, which should better enforce the stabilization of FE HZO in the *o*-phase.

Indeed, the XRD measurements of HZO2 and HZO3 samples in Fig. 3(a) clearly indicate the stabilization of the o-HZO phase, coexisting in varying amounts with the *m*-HZO phase ($P2_1/c$ - PDF 04–002-5428). Actually, an asymmetry of the main peak at ∼30° is evident and indicates the coexistence of both orthorhombic and monoclinic phases, with their characteristic signatures *o*-(111) at 29.9° and *m*-(−111) at 28.3°. The thickness of the layers extracted from the fit of the diffraction patterns are given in Supplemental Material Fig. S1 [46]. This illustrates the challenges of accurate quantitative estimation of crystalline phases by relying only on XRD, especially in the case of ultrathin interfaces. On the other hand, XPS readily disentangles the exact amount of *o* and *m* phases.

More exactly, the asymmetry in the O 1s XPS line developing toward HBE confirms the assignment of the HBE component to oxygens in the polar sublattice of *o*-HZO and the LBE at 529.0 eV–529.3 eV component to O in the non-polar sublattice, possibly coexisting with other non-polar phases such as *m*-HZO.

The smaller experimental CLS of 0.43 eV–0.63 eV of the HBE components compared to the theoretical derived one of ∼0.8 eV derive from a number of factors such as phase mixing of polar and non-polar environment [63] and local stoichiometry alteration due to defects and oxygen or cation vacancies, which may smooth out the potential contrast responsible for CLSs.

Moreover, final state effects describing how the system responds after the photoelectron is ejected are expected to contribute to the difference between theoretical and experimental CLS more than initial state effects, due to weakly interacting electrons in the O 1s core level and on the other hand due to stronger dynamic screening. It has been established [64–66] that ultrathin films may experience interface-induced screening from the substrate that significantly reduces core-level binding energy shifts compared to values predicted from DFT close to the metallic substrates. Moreover, image charge formation [67], by reducing the energy difference between core levels at inequivalent sites, may

additionally reduce the observed CLS compared to the experimental ones.

However, the CLSs calculated for the other relevant crystalline phases (cubic, tetragonal, and monoclinic) lie in the opposite direction, toward lower binding energies compared to the polar phase (Fig. 2). This aspect is reassuring that the identified shifts identified in our XPS experiment describe the two different, polar and non-polar phases.

From the individual analysis of O 1s spectra for HZO2 [Fig. 3(c)] and HZO3 [Fig. 3(d)], we can extract the exact amount of the *o*-HZO and *m*-HZO phases presented in Table I.

We observe that in the 3 nm HZO2 sample, there is still an appreciable amount (∼24%) of *m*-HZO phase while it sharply drops in the thicker, 5 nm one—HZO3 to 7%.

This behavior is consistent with the previous reports demonstrating the role of electrode conductivity in enhancing polarization and minimizing depolarization fields at the interface [13,47,48].

The increase in the amount of the FE phase in the form of *o*-HZO in the thicker film is explained by the reduced impact of interfacial dead layers when going from 3 nm to 5 nm thickness, enhancing the stabilization of the ferroelectric orthorhombic phase in HZO3. Thus, while higher LSMO conductivity ($x = 0.33$) promotes orthorhombic phase stabilization via enhanced interfacial screening, the thickness-dependent reduction in monoclinic fraction observed between HZO2 and HZO3 arises from intrinsic thickness effects rather than electrode properties. Once the electrode doping is fixed, the evolution of phase composition is governed mainly by the diminishing influence of interfacial dead layers and the enhanced retention of the orthorhombic phase in slightly thicker HZO. This trend is well supported by the previous results, which show that dielectric permittivity increases with thickness due to improved ferroelectric phase retention and diminished interfacial suppression effects [49]. Our electrical measurements given in the Supplemental Material [46], consistent with this observation, display the same trend, with the sample containing the largest amount of *m*-HZO phase displaying no ferroelectric behaviour, while the increase of the ferroelectric signal is well correlated with the increase in the *o*-HZO phase.

IV. CONCLUSIONS

Our work establishes a robust and accessible spectroscopic protocol to distinguish and quantify the polar (ferroelectric) and non-polar phases of $HfZrO_2$ thin films through detailed analysis of the O 1s XPS spectra. In contrast to conventional phase identification via XRD—often compromised by overlapping signals from substrates or buffer layers in nanoscale films—our approach offers a surface-sensitive and phase-selective alternative, suitable for routine characterization even in complex heterostructures.

By combining first-principles core-level shift calculations, which include both initial and final state effects, with experimental XPS data, we demonstrate that the O 1s peak contains distinct, well-resolved spectral components. Oxygen atoms in the polar sublattice of the orthorhombic, ferroelectric phase contribute at higher binding energies (HBEs), while those in symmetric, non-polar environments—including monoclinic HZO—appear up to 0.8 eV toward lower binding energies (LBEs). These features are separated by over 1 eV from contamination-related signals, enabling unambiguous deconvolution even with standard laboratory X-ray sources.

This spectral separation forms the basis for quantitative phase analysis, allowing us to directly determine the proportion of ferroelectric and non-ferroelectric phases in HZO films. By generalizing this insight, we classify all non-polar hafnia-based phases within the LBE component, facilitating broader application of the method across hafnia-based oxides.

Finally, by correlating our spectroscopic results with XRD and electrical measurements across a series of HZO films with varying phase composition, we validate the reliability of the method and further highlight the interplay between the ferroelectric phase and the adjacent metallic electrode. Our findings thus provide both a fundamental spectroscopic fingerprint of ferroelectricity in CMOS-compatible oxides and a practical metrology tool for guiding the design and integration of next-generation ferroelectric devices.

This approach offers a powerful and scalable route for phase-engineering and characterization of hafnia-based ferroelectrics, accelerating the deployment of non-volatile memory, steep-slope transistors, and neuromorphic computing architectures within existing CMOS platforms.

ACKNOWLEDGMENTS

This work was funded by the Romanian UEFISCDI Agency under Grant No. 44PCE/2025 (PN-IV-P1-PCE-2023–1830). C.C. acknowledges the financial support from the PNRR project under Grant No. 760239/28.12.2023, funded by the Romanian Ministry of Research, Innovation, and Digitization through the National Recovery and Resilience Plan. The experiments were performed using the National Interest Setup "System of complex XPS/ESCA installations and research using synchrotron radiation."

DATA AVAILABILITY

The data that support the findings of this article are not publicly available. The data are available from the authors upon reasonable request.

[1] Y. Shen, K. Ooe, X. Yuan, T. Yamada, S. Kobayashi, M. Haruta, D. Kan, and Y. Shimakawa, Ferroelectric freestanding hafnia membranes with metastable rhombohedral structure down to 1-nm-thick, Nat. Commun. **15**, 4789 (2024).

[2] Y. E. Li *et al.*, Improper ferroelectricity at the monolayer limit, arXiv:2503.06214.

[3] S. Lv, T. Cao, Z. Wang, T. Xie, S. Gao, G. Teobaldi, Q. Hu, and L.-M. Liu, Physical origin of hafnium-based ferroelectricity, Comput. Mater. Today **4**, 100010 (2024).

[4] O. Ohtaka, H. Fukui, T. Kunisada, T. Fujisawa, K. Funakoshi, W. Utsumi, T. Irifune, K. Kuroda, and T. Kikegawa, Phase

relations and volume changes of Hafnia under high pressure and high temperature, J. Am. Ceram. Soc. **84**, 1369 (2004).

[5] Y. Wei *et al.*, A rhombohedral ferroelectric phase in epitaxially strained $Hf_{0.5}Zr_{0.5}O_2$ thin films, Nat. Mater. **17**, 1095 (2018).

[6] H. Aramberri and J. Íñiguez, Theoretical approach to ferroelectricity in hafnia and related materials, Commun. Mater. **4**, 95 (2023).

[7] T. Zhu, L. Ma, S. Deng, and S. Liu, Progress in computational understanding of ferroelectric mechanisms in HfO_2, npj Comput. Mater. **10**, 188 (2024).

[8] M. H. Park, T. Schenk, C. M. Fancher, E. D. Grimley, C. Zhou, C. Richter, J. M. LeBeau, J. L. Jones, T. Mikolajick, and U. Schroeder, A comprehensive study on the structural evolution of HfO_2 thin films doped with various dopants, J. Mater. Chem. C Mater. Opt. Electron. Devices **5**, 4677 (2017).

[9] U. Schroeder *et al.*, Lanthanum-doped hafnium oxide: A robust ferroelectric material, Inorg. Chem. **57**, 2752 (2018).

[10] U. Schroeder, M. H. Park, T. Mikolajick, and C. S. Hwang, The fundamentals and applications of ferroelectric HfO_2, Nat. Rev. Mater. **7**, 653 (2022).

[11] K. Park *et al.*, Atomic-scale scanning of domain network in the ferroelectric HfO_2 thin film, ACS Nano **18**, 26315 (2024).

[12] S. Shi *et al.*, Interface-engineered ferroelectricity of epitaxial $Hf_{0.5}Zr_{0.5}O_2$ thin films, Nat. Commun. **14**, 1780 (2023).

[13] S. Estandía, J. Gàzquez, M. Varela, N. Dix, M. Qian, R. Solanas, I. Fina, and F. Sánchez, Critical effect of the bottom electrode on the ferroelectricity of epitaxial $Hf_{0.5}Zr_{0.5}O_2$ thin films, J. Mater. Chem. C Mater. Opt. Electron. Devices **9**, 3486 (2021).

[14] X. Xu, F.-T. Huang, Y. Qi, S. Singh, K. M. Rabe, D. Obeysekera, J. Yang, M.-W. Chu, and S.-W. Cheong, Kinetically stabilized ferroelectricity in bulk single-crystalline HfO_2:Y, Nat. Mater. **20**, 826 (2021).

[15] G. Li, S. Yan, Y. Liu, W. Zhang, Y. Xiao, Q. Yang, M. Tang, J. Li, and Z. Long, Unraveling the origins of ferroelectricity in doped hafnia through carrier-mediated phase transitions, npj Comput. Mater. **11**, 34 (2025).

[16] N. Kaiser, Y.-J. Song, T. Vogel, E. Piros, T. Kim, P. Schreyer, S. Petzold, R. Valentí, and L. Alff, Crystal and electronic structure of oxygen vacancy stabilized rhombohedral hafnium oxide, ACS Appl. Electron. Mater. **5**, 754 (2023).

[17] N. Kaiser, T. Vogel, A. Zintler, S. Petzold, A. Arzumanov, E. Piros, R. Eilhardt, L. Molina-Luna, and L. Alff, Defect-stabilized substoichiometric polymorphs of hafnium oxide with semiconducting properties, ACS Appl. Mater. Interfaces **14**, 1290 (2022).

[18] J.-H. Yuan, G.-Q. Mao, K.-H. Xue, N. Bai, C. Wang, Y. Cheng, H. Lyu, H. Sun, X. Wang, and X. Miao, Ferroelectricity in HfO_2 from a coordination number perspective, Chem. Mater. **35**, 94 (2023).

[19] H.-J. Lee, M. Lee, K. Lee, J. Jo, H. Yang, Y. Kim, S. C. Chae, U. Waghmare, and J. H. Lee, Scale-free ferroelectricity induced by flat phonon bands in HfO_2, Science **369**, 1343 (2020).

[20] M. Materano, T. Mittmann, P. D. Lomenzo, C. Zhou, J. L. Jones, M. Falkowski, A. Kersch, T. Mikolajick, and U. Schroeder, Influence of oxygen content on the structure and reliability of ferroelectric $Hf_xZr_{1-x}O_2$ layers, ACS Appl. Electron. Mater **2**, 3618 (2020).

[21] B. Noheda, P. Nukala, and M. Acuautla, Lessons from hafnium dioxide-based ferroelectrics, Nat. Mater. **22**, 562 (2023).

[22] N. A. Hill, Why are there so few magnetic ferroelectrics? J. Phys. Chem. B **104**, 6694 (2000).

[23] T. S. Böscke, S. Teichert, D. Bräuhaus, J. Müller, U. Schröder, U. Böttger, and T. Mikolajick, Phase transitions in ferroelectric silicon doped hafnium oxide, Appl. Phys. Lett. **99**, 112904 (2011).

[24] D. Martin *et al.*, Ferroelectricity in Si-doped HfO_2 revealed: A binary lead-free ferroelectric, Adv. Mater. **26**, 8198 (2014).

[25] S. Mueller, J. Mueller, A. Singh, S. Riedel, J. Sundqvist, U. Schroeder, and T. Mikolajick, Incipient ferroelectricity in Al-doped HfO_2 thin films, Adv. Funct. Mater. **22**, 2412 (2012).

[26] Y. Yun *et al.*, Intrinsic ferroelectricity in Y-doped HfO_2 thin films, Nat. Mater. **21**, 903 (2022).

[27] J. Müller, T. S. Böscke, U. Schröder, S. Mueller, D. Bräuhaus, U. Böttger, L. Frey, and T. Mikolajick, Ferroelectricity in simple binary ZrO_2 and HfO_2, Nano Lett. **12**, 4318 (2012).

[28] S. Zhou, J. Zhang, and A. M. Rappe, Strain-induced antipolar phase in hafnia stabilizes robust thin-film ferroelectricity, Sci. Adv. **8**, eadd5953 (2022).

[29] T. Li, J. Dong, N. Zhang, Z. Wen, Z. Sun, Y. Hai, K. Wang, H. Liu, N. Tamura, S. Mi, S. Chengg, C. Ma, Y. He, L. Li, S. Kei, H. Huangj, and Y. Cao, Interface control of tetragonal ferroelectric phase in ultrathin Si-doped HfO_2 epitaxial films, Acta Mater. **207**, 116696 (2021).

[30] M. H. Park, Y. H. Lee, T. Mikolajick, U. Schroeder, and C. S. Hwang, Thermodynamic and kinetic origins of ferroelectricity in fluorite structure oxides, Adv. Electron. Mater. **5**, 1800522 (2019).

[31] P. Giannozzi *et al.*, QUANTUM ESPRESSO: A modular and open-source software project for quantum simulations of materials, J. Phys. Condens. Matter **21**, 395502 (2009).

[32] P. Giannozzi *et al.*, Advanced capabilities for materials modelling with QUANTUM ESPRESSO, J. Phys. Condens. Matter **29**, 465901 (2017).

[33] J. P. Perdew and A. Zunger, Self-interaction correction to density-functional approximations for many-electron systems, Phys. Rev. B **23**, 5048 (1981).

[34] A. Dal Corso, Pseudopotentials periodic table: From H to Pu, Comput. Mater. Sci. **95**, 337 (2014).

[35] A. Jain *et al.*, Commentary: The Materials Project: A materials genome approach to accelerating materials innovation, APL Mater. **1**, 011002 (2013).

[36] H. J. Monkhorst and J. D. Pack, Special points for Brillouin-zone integrations, Phys. Rev. B **13**, 5188 (1976).

[37] K. Momma and F. Izumi, *VESTA 3* for three-dimensional visualization of crystal, volumetric and morphology data, J. Appl. Crystallogr. **44**, 1272 (2011).

[38] B. O. Koopman, Hamiltonian systems and transformation in Hilbert space, Proc. Natl. Acad. Sci. USA **17**, 315 (1931).

[39] S. Tardio and P. J. Cumpson, Practical estimation of XPS binding energies using widely available quantum chemistry software, Surf. Interface Anal. **50**, 5 (2018).

[40] J. N. Andersen, D. Hennig, E. Lundgren, M. Methfessel, R. Nyholm, and M. Scheffler, Surface core-level shifts of some 4*d*-metal single-crystal surfaces: Experiments and *ab initio* calculations, Phys. Rev. B **50**, 17525 (1994).

[41] W. F. Egelhoff Jr, Core-level binding-energy shifts at surfaces and in solids, Surf. Sci. Rep. **6**, 253 (1987).

[42] M. K. Horton *et al.*, Accelerated data-driven materials science with the Materials Project, Nat. Mater. **24**, 1522 (2025).

[43] I. Petousis, D. Mrdjenovich, E. Ballouz, M. Liu, D. Winston, W. Chen, T. Graf, T. D. Schladt, K. A. Persson, and F. B. Prinz, High-throughput screening of inorganic compounds for the discovery of novel dielectric and optical materials, Sci. Data **4**, 160134 (2017).

[44] U. Schroeder, C. S. Hwang, and H. Funakubo, *Ferroelectricity in Doped Hafnium Oxide: Materials, Properties and Devices* (Woodhead Publishing, Sawston, Cambridge, Cambridgeshire, UK, 2019).

[45] T. Mittmann *et al.*, Origin of ferroelectric phase in undoped HfO_2 films deposited by sputtering, Adv. Mater. Interfaces **6**, 1900042 (2019).

[46] See Supplemental Material at http://link.aps.org/supplemental/10.1103/h2lj-slbg for thickness extraction from XRD fits (Fig. S1), electrical characterization (Fig. S3), and supporting discussion including Refs. [47–49].

[47] R. Koduru, A. K. Saha, M. M. Frank, and S. K. Gupta, Small-signal capacitance in ferroelectric hafnium zirconium oxide: Mechanisms and physical insights, Nanoscale **17**, 6154 (2025).

[48] R. Alcala, M. Materano, P. D. Lomenzo, P. Vishnumurthy, W. Hamouda, C. Dubourdieu, A. Kersch, N. Barrett, T. Mikolajick, and U. Schroeder, The electrode-ferroelectric interface as the primary constraint on endurance and retention in HZO-based ferroelectric capacitors, Adv. Funct. Mater. **33**, 2303261 (2023).

[49] S. Oh, H. Kim, A. Kashir, and H. Hwang, Effect of dead layers on the ferroelectric property of ultrathin $HfZrO_x$ film, Appl. Phys. Lett. **117**, 252906 (2020).

[50] L. C. Tănase *et al.*, Polarization orientation in lead zirconate titanate (001) thin films driven by the interface with the substrate, Phys. Rev. Appl. **10**, 034020 (2018).

[51] D. G. Popescu, N. Barrett, C. Chirila, I. Pasuk, and M. A. Husanu, Influence of hole depletion and depolarizing field on the $BaTiO_3$ $La_{0.6}Sr_{0.4}MnO_3$ interface electronic structure revealed by photoelectron spectroscopy and first-principles calculations, Phys. Rev. B **92**, 235442 (2015).

[52] D. G. Popescu *et al.*, Experimental Band Structure of $Pb(Zr, Ti)O_3$: Mechanism of ferroelectric stabilization, Adv. Sci. **10**, e2205476 (2023).

[53] M.-A. Husanu *et al.*, Ferroelectricity modulates polaronic coupling at multiferroic interfaces, https://doi.org/10.21203/rs.3.rs-1208929/v1.

[54] D. G. Popescu, M. A. Husanu, C. Chirila, L. Pintilie, and C. M. Teodorescu, Impact on ferroelectricity and band alignment of gradually grown Au on $BaTiO_3$, Phys. Stat. Solidi. Rapid Res. Lett. **13**, 1900077 (2019).

[55] D. G. Popescu, M. A. Husanu, C. Chirila, L. Pintilie, and C. M. Teodorescu, The interplay of work function and polarization state at the Schottky barriers height for $Cu/BaTiO_3$ interface, Appl. Surf. Sci. **502**, 144101 (2020).

[56] C. A. F. Vaz, J. Hoffman, Y. Segal, J. W. Reiner, R. D. Grober, Z. Zhang, C. H. Ahn, and F. J. Walker, Origin of the magnetoelectric coupling effect in $Pb(Zr_{0.2}Ti_{0.8})O_3/La_{0.8}Sr_{0.2}MnO_3$ multiferroic heterostructures, Phys. Rev. Lett. **104**, 127202 (2010).

[57] E. Dagotto, T. Hotta, and A. Moreo, Colossal magnetoresistant materials: The key role of phase separation, Phys. Rep. **344**, 1 (2001).

[58] M. A. Huşanu, D. G. Popescu, C. A. Tache, N. G. Apostol, A. Barinov, S. Lizzit, P. Lacovig, and C. M. Teodorescu, Photoelectron spectroscopy and spectro-microscopy of $Pb(Zr, Ti)O_3$ (111) thin layers: Imaging ferroelectric domains with binding energy contrast, Appl. Surf. Sci. **352**, 73 (2015).

[59] C. M. Teodorescu, Self-consistently derived sample permittivity in stabilization of ferroelectricity due to charge accumulated at interfaces, Phys. Chem. Chem. Phys. **24**, 5419 (2022).

[60] D. G. Popescu, M. A. Huşanu, L. Trupină, L. Hrib, L. Pintilie, A. Barinov, S. Lizzit, P. Lacovig, and C. M. Teodorescu, Spectro-microscopic photoemission evidence of charge uncompensated areas in $Pb(Zr, Ti)O_3$(001) layers, Phys. Chem. Chem. Phys. **17**, 509 (2015).

[61] L. Pintilie *et al.*, Polarization induced self-doping in epitaxial $Pb(Zr_{0.20}Ti_{0.80})O_3$ thin films, Sci. Rep. **5**, 1 (2015).

[62] C. F. Chirila, V. Stancu, G. A. Boni, I. Pasuk, L. Trupina, L. D. Filip, C. Radu, I. Pintilie, and L. Pintilie, Controlling polarization direction in epitaxial $Pb(Zr_{0.2}Ti_{0.8})O_3$ films through Nb (n-type) and Fe (p-type) doping, Sci. Rep. **12**, 755 (2022).

[63] C. F. Chirila, G. A. Boni, D. G. Popescu, C. M. Istrate, M. A. Husanu, L. D. Filip, C. Besleaga, L. Pintilie, and A. Dimoulas, Ferroelectric $Hf_{0.5}Zr_{0.5}O_2$ thin films on TiN/Si substrates grown by pulsed laser deposition at CMOS-compatible temperatures, Ceram. Int. **51**, 50941 (2025).

[64] S. Hufner, *Photoelectron Spectroscopy* (Springer, Berlin, Germany, 2010).

[65] D. A. Ivanov, P. M. Ostrovsky, and M. A. Skvortsov, Correlations of the local density of states in quasi-one-dimensional wires, Phys. Rev. B **79**, 205108 (2009).

[66] T. Mizokawa, A. Fujimori, T. Arima, Y. Tokura, N. Mori, and J. Akimitsu, Electronic structure of $PrNiO_3$ studied by photoemission and x-ray-absorption spectroscopy: Band gap and orbital ordering, Phys. Rev. B **52**, 13865 (1995).

[67] C. M. Teodorescu, Image molecular dipoles in surface enhanced Raman scattering, Phys. Chem. Chem. Phys. **17**, 21302 (2015).